

## A REVIEW OF MICROMECHANICS OF FAILURE WAVES IN SILICATE GLASSES

N. SINGH BRAR and H.D. ESPINOSA

*Impact Physics Laboratory, University of Dayton Research Institute,  
Dayton, OH 45469-0182, USA*

*Aeronautics and Astronautics, Purdue University, West Lafayette, IN,  
17007-1282, USA*

Three mechanisms have been proposed for the recently observed failure waves (fronts) in plate impact experiments on silicate glasses. The first based on the phase transformation in glass does not explain the observed features in measured wave profiles. The second involves the comparison of the transfer of elastic shear strain energy in glass specimen due to 1-D compression to dilatant strain energy as a result of microcracking. No simulations of wave profiles were performed using this mechanism. The third is based on the microcracking multiple-plane model and is very rigorously derived. Numerical simulations of the measured wave profiles were carried out following the model. The simulations show that the failure wave phenomenon can be modeled by propagating surfaces of discontinuity from the specimen surface to its interior. Lateral stress increase and reduction of spall strength behind the failure front are successfully predicted by the multiple-plane model. Numerical simulations of high strain rate pressure shear experiments indicate the model predicts reasonably well the shear resistance of the material at strain rates as high as  $1 \cdot 10^6$  m/s. The agreement is believed to be the result of the capability of the model in simulating damage-induced anisotropy. By examining the kinetics of the failure process in plate experiments, it is shown that the progressive glass spallation in the vicinity of the failure front and the rate of increase in lateral stress are more consistent with a representation of inelasticity based on shear-activated flow surfaces and microcracking, rather than pure microcracking. In the former mechanism, microcracks are likely formed at a later time at the intersection of flow surfaces.

(Received December 5, 1996)

## 1. INTRODUCTION

A number of investigators have confirmed that a failure (fracture) wave propagates behind the elastic wave in silicate and metallic (filled) glasses under shock compression in 1-D strain plate impact experiments. The failure wave is defined as a wave or front propagating into shock stressed glass ahead of which the material is intact and behind which the material has lost shear strength considerably. Kanel et al. [1,2] reported that a failure wave propagates in shock loaded window (K8 and K19) glasses at stresses near or below the HEL at a speed of approximately 1.5 - 2 km/s. A small recompression on top of the free surface velocity-time profile was produced as a result of the interaction between the unloading wave from the rear surface of the target and the advancing failure wave. The material behind the failure wave was postulated to have a network of cracks initiated by the compression which lowered the impedance and reduced the spall strength to zero. They also observed a dramatic increase in the lateral stress in K8 glass specimens on arrival of the failure wave, measured by lateral stress gauge indicating considerable loss of shear strength of the material behind the failure wave. Both of these observations were numerically simulated assuming that the failure wave velocity decreases with the propagation distance in the specimen.

Brar et al. [3-6] performed a comprehensive study of the spall behavior of soda lime glass in terms of the location of the spall plane with respect to the failure wave front in order to probe the tensile strength of the material in front of and behind the failure wave. Using manganin stress gauges for stress measurement, they found that under a compressive shock loading of 7 GPa the spall strength of soda lime glass was approximately 3.8 GPa in the region of the specimen ahead of the failure wave, whereas, the region behind the failure wave had negligibly small spall strength. The failure wave velocity was determined, from the arrival times in lateral stress gauge profiles to be  $2.2 \pm 0.2$  km/s. The lowest or threshold shock stress at which the formation of failure wave occurred in soda lime glass specimens was 3.8 GPa. The shear strength ( $\tau = 0.5(\sigma_x - \sigma_y)$ ) of soda lime glass behind the failure wave at shock stresses close to the HEL (6 - 7 GPa) dropped dramatically from 2.1 GPa to 1 GPa. Espinosa and Brar [7] performed lateral stress gauge experiments on aluminosilicate glass and found similar results.

Raiser et al. [8] measured the spall strength of aluminosilicate glass specimens shock loaded to 8.4 GPa, in regions in front of and behind the failure wave using VISAR. They found that the spall strength of in the regions in front of the failure wave was as high as 4.4 GPa. In regions behind the failure wave in a shot conducted at 7.5 - 7.9 GPa the spall strength was almost zero. They also found that the lower threshold level of

shock stress required to generate a failure wave in aluminosilicate glass specimens was 3.5 GPa. Raiser [9] also attempted to probe the optical properties (e.g., refractive index) of the failed glass behind the failure wave using a laser beam reflecting off the impact surface of the target plate. They have found that the laser beam disappears as soon as the failure wave forms at the impact surface. Furthermore, they did not find any evidence to suggest that the formation of the failure wave was related to the impact surface roughness of the plate specimen.

Recently, Bourne et al. [10-12] have performed a detailed study on soda lime, borosilicate and filled (metal) glasses to measure the HEL and the shear strength of the material behind and in front of the failure wave using manganin stress gauges. Lateral gauge stress profiles for shock levels above a threshold comprise two stress levels. The jump in lateral stress occurs when the failure wave crosses the gauge position. The results on shear strength of soda lime glass agree with those of Brar et al. [6] up to HEL and also show that the shear strength of the material in front of the failure wave is constant (2 GPa) above the HEL suggesting the elasto-plastic behavior. The failure wave velocity was reported to increase with increasing shock stresses. In the range of shock stresses from 4 - 7 GPa failure wave velocity was measured to be in the range 2.2 - 2.6 km/s. These investigators obtained further evidence of the failure waves in shock loaded soda lime glass specimen through high speed photography [13]. A sequence of high speed photographs taken with a framing camera on soda lime glass targets showed several dark regions developing between the shock front and the failure front. The appearance of these dark regions was explained on the basis of local structural collapse occurring at inhomogeneities within the microstructure. In all three types of glasses, they found the lowest threshold longitudinal stress level at which the failure wave is observed to form. In the case of filled glass both the lowest and highest threshold stress values were found to be 0.8 and 2.0 times the HEL, respectively [12].

Dandekar and Beaulieu [14] performed a series of shock compression experiments on soda lime glass specimens from the same lot as used by Brar et al. They found that the failure wave is initiated at longitudinal stress levels between 4.7 GPa and 5.2 GPa. The failure wave was measured as propagating at a velocity of  $1.56 \pm 0.07$  km/s in specimens of thickness varying between 3.1 and 9.4 mm at a shock stress of 5.2 GPa. The shock and release impedances of glass in the region traversed by the failure wave were determined to be 4.1 and 5.13 Gg/m<sup>3</sup>, respectively. These investigators have also observed the disappearance of the laser beam used to probe the material on arrival of the failure wave as reported by Raiser [9].

Grady [15-16] measured stress wave profiles of soda lime glass specimens shock loaded to stress levels of up to 20 GPa using VISAR. The shock compression stress-time profiles at shock stress levels below HEL

(4-7 GPa) are very unstable. The profiles for shock stress levels above 10 GPa are much more smooth showing a ramp like elastic portion followed by a relatively steep shock wave. He postulated that the unstable stress levels for wave profiles between 4 and 7 GPa are due to the failure of the material as a result of the formation of the failure wave.

## 2. EXPERIMENTAL METHODS AND RESULTS

### 2.1. Wave Interaction Experiments

In these experiments, glass plate specimens with or without low impedance backing plate (PMMA) are impacted by a flyer plate of known Hugoniot launched from a compressed gas or powder gun. The interaction of the unloading stress wave from the free surface or glass/PMMA interface with the advancing failure wave is observed as a slight recompression on top of the stress wave. The recompression in manganin gauge profile observed by Brar et al. [6] in a shocked soda lime glass specimen is shown in Fig. 1, *a*. Figure 1, *b* shows the recompression in free surface velocity measurements on K-19 glass specimens using VISAR by Kanel et al. and Fig. 1, *c* in soda lime glass specimens by Dandekar and Beaulieu [14].

### 2.2. Spall Strength Experiments

Brar et al. [3-6] configured the soda lime glass targets to measure the spall strength of the material in regions of the target in front of and behind the failure wave with manganin gauges. In one set of experiments, the target geometry was configured in such a way that the spall plane was behind the failure wave, assuming the failure wave speed to be 2 km/s. In these experiments the spall strength of glass specimens shocked in the stress range of 4-7 GPa was found to be negligible small. In the second set of experiments, the spall plane was configured to be in front of the failure wave and in this case they found the gauge profile showed complete unloading without any signs of spall at stress levels to 7 GPa.

Raiser et al. [8] designed aluminosilicate glass targets to perform similar spall strength measurements using VISAR. They found that when the glass specimens are subjected to a sufficiently large compressive stress 8.4 GPa the spall strength in the region where the failure wave has not propagated is as high as 4.4 GPa as shown in Fig. 2. In a similar experiment at 7.5 - 7.9 GPa shock stress the spall strength in regions of the specimen where failure wave has propagated through spall strength is almost zero. At the lower shock stresses of 3.4 GPa the spall strength is retained in the same region of the specimen because the failure wave does not form at these lower shock stresses.

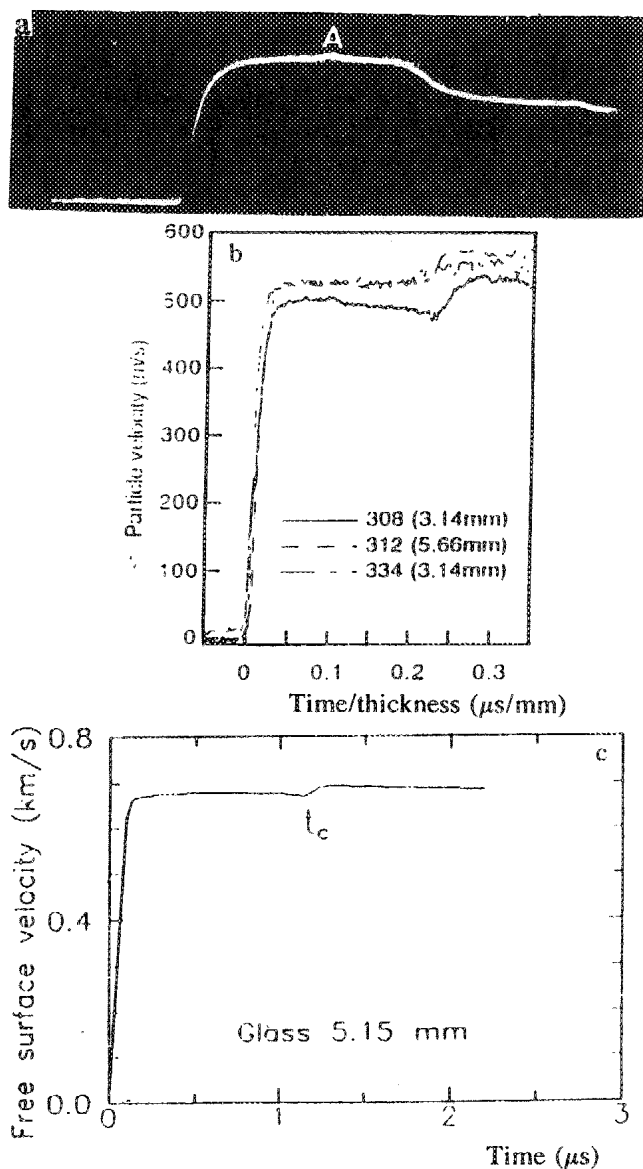


FIGURE 1. Wave profiles showing recompression as a result of the interaction of advancing failure wave and unloading wave from the rear surface of the target from different investigations: (a) shot 7-1628 on soda lime glass (point A) [6], scales: 0.5 V/div and 0.5  $\mu\text{s}/\text{div}$ ; (b) soda lime glass [14]; (c) K-19 glass [1].

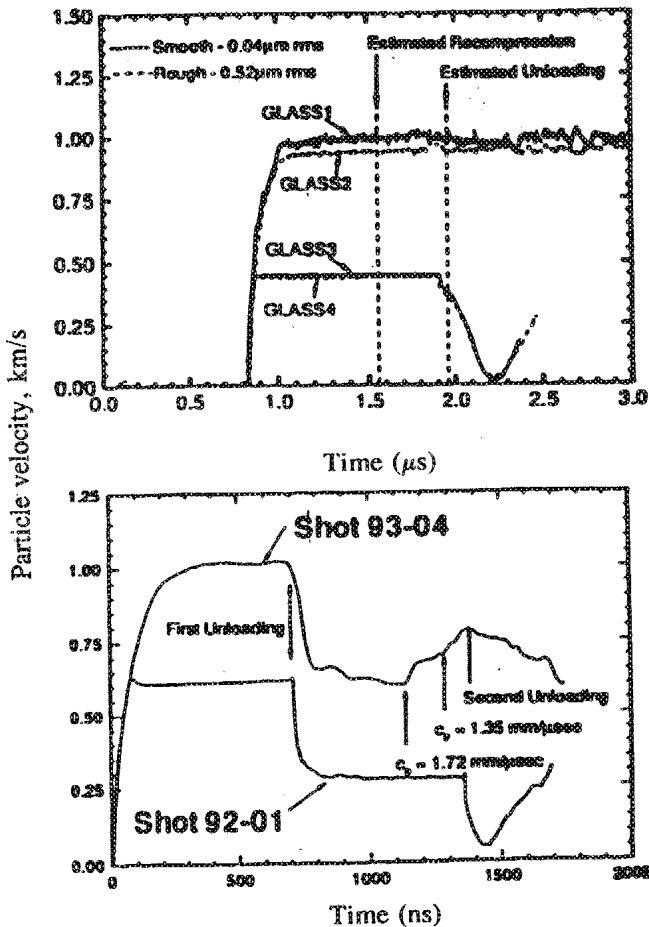


FIGURE 2. (above) Free surface velocity — time profiles for shots GLASS1 to GLASS4 in which the spall plane is *behind* the failure wave. (below) Free surface velocity — time profiles for shots 92-01 and 93-04 in which the spall plane is *in front* of the failure wave [8].

### 2.3. Lateral Gauge Experiments

In this technique a manganin stress gauge is embedded between two glass plates in the lateral or transverse orientation to the shock direction as shown schematically in Fig.3. The lateral gauge profile shows a dramatic increase in the stress level on arrival of the failure wave at the gauge location. The

lateral gauge profiles obtained by different investigators in different types of glasses are shown in Fig.4.

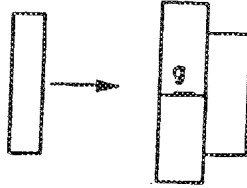


FIGURE 3. Schematic of the target configuration with an embedded lateral manganin gauge.

#### 2.4. High Speed Photography Experiments

Bourne et al. [13] measured failure wave speeds in soda lime and Pyrex glass specimens using the Ultramac FS501 high speed camera. The shock and failure fronts were viewed in the shadowgraph mode through one of the polished faces of the target with a parallel light beam directed in a direction parallel to the shock front.

### 3. MECHANISMS OF FAILURE WAVES

The structure of the measured shock wave profiles reflect the processes involved in dynamic failure under shock compression through volume change that takes place under mean stress accompanied by the inelastic failure of the material due to intense shear stress developed during compressive loading. Plasticity and fracture are both viable mechanisms for inelastic deformation which takes place in shock compression and their relative contribution depends strongly on the type of material and loading conditions. The fact that failure waves in glass are observed at shock stress levels below the HEL pose a challenge to our conventional understanding of the failure processes which lead to dynamic failure. The longitudinal stress or particle velocity in the shocked specimen undergoes little or no change on both sides of the failure waves and thus imposes the condition of zero volume change during the process. The observed loss of dynamic shear and tensile strengths of the material behind the failure wave must take place through a combination of plastic and fracturing processes under the confinement of mean stress.

Three plausible mechanisms have been proposed for the formation of failure waves. The first one, due to Clifton [17], is based on phase transformation of silica glass to known high density silica phases observed under shock compression. Another mechanism has been proposed by Grady [18] who has based his analysis on comparing the transfer of elastic shear strain

energy to dilatant strain energy due to microcracking. Espinosa [19] and

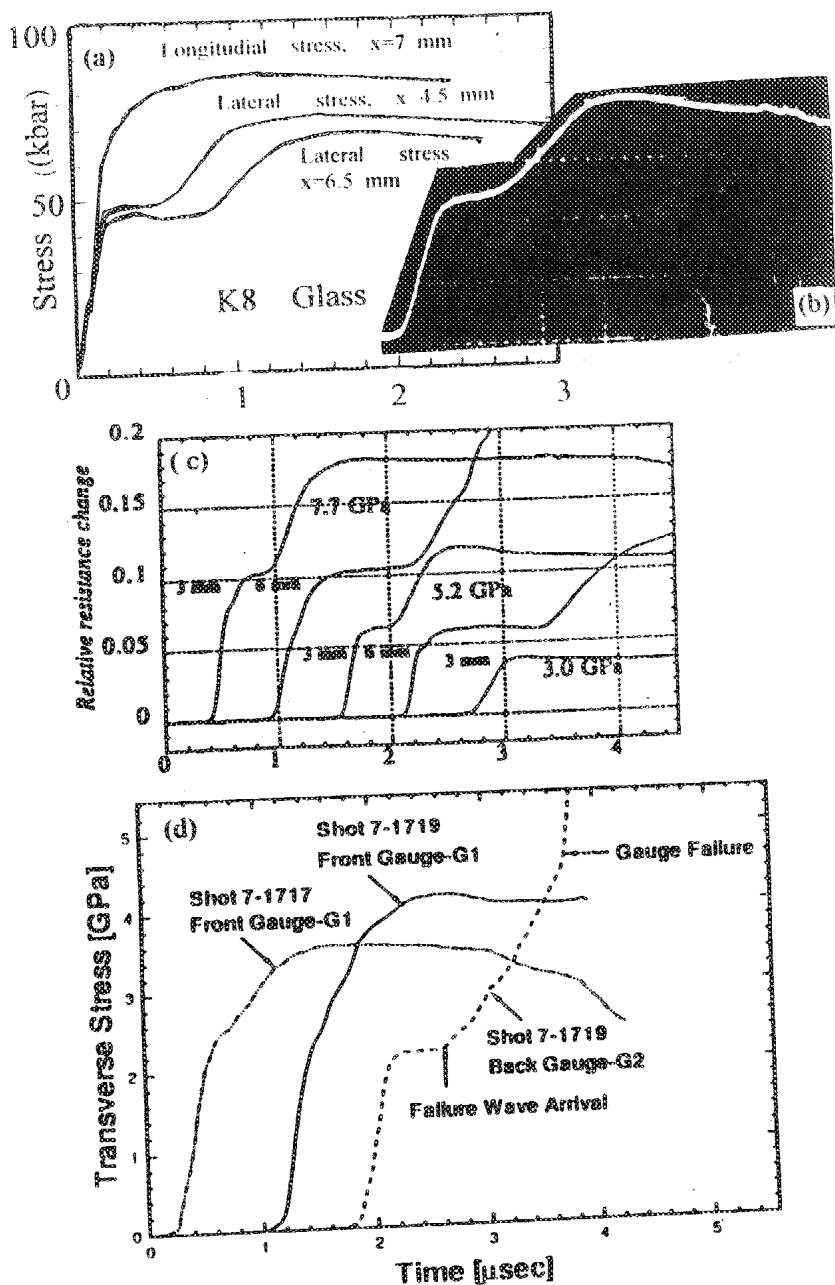


FIGURE 4. Lateral gauge profiles in (a) K8 glass [1], (b) soda lime glass [6], (c) soda lime glass [10,11], and (d) aluminosilicate glass [38].



Espinosa et al. [20] have proposed a third mechanism in which the failure wave is hypothesized to be due to the inhomogeneous inelastic behavior of silicate glasses containing the network modifiers.

### 3.1. Phase Transformation

In the analysis of the observed features of failure waves, Clifton [17] raised the fundamental question about extensive cracking of the specimen being responsible for the failure front or wave, as proposed by Kanel [1,2], under the uniaxial strain compression. How can any crack open in the material under compression? Secondly, why does failure at the impact surface begin immediately, but in the interior of the specimen the same compressive state is supported for an extended time prior to failure? In view of these fundamental constraints, he proposed that the failure wave corresponds to a propagating phase boundary, similar to a transformation shock. The phase boundary formed is likely due to the phase transformation of silica to a crystalline phase or denser phases like coesite or stishovite. There have been numerous studies on these phase transformations in shocked silica glass and crystalline quartz in shock wave literature. He argued that the large strains involved in phase transformations is likely to induce microcracking as a result of heterogeneous nucleation and growth of transformed regions. This microcracking could explain the observed loss of spall strength.

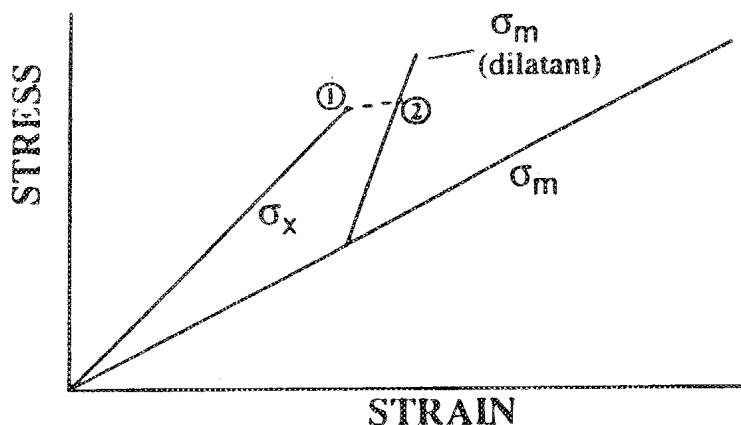


FIGURE 5. Transition state for failure waves in brittle solids. In each example the shock state at point one is below the Hugoniot elastic limit,  $\sigma_x$  and  $\sigma_m$  represent uniaxial strain and mean stress loading paths, respectively [18].

There are two major problems with the above proposed phase transformation hypothesis for the origin of the failure wave. The first is that the

phase transformation must be accompanied by a discontinuity in density or volume of the material. Such a discontinuity would mean a discontinuity in longitudinal stress or particle velocity on arrival of the failure wave which has not been observed in any of the studies summarized in Section 1. The second problem is that starting material in all the phase transformations studies on silica under shock was either silica glass or crystalline quartz and not soda lime glass. In one study due to Gibbons and Aherns [21] where soda lime glass was subjected to shock compression, very slight permanent increase in the refractive index was observed to take place at stress levels above 4.0 GPa (increase of 0.01 at 8 GPa). The threshold shock stress level of 4.0 GPa for the slight permanent change in refractive index or density of soda lime glass does correspond to the threshold stress of 3.8 GPa above which the failure waves have been observed. The analysis does not establish the relationship between the transformation shock and failure wave with certainty, because of the lack of information on the equation of state of glass at higher shock stress levels.

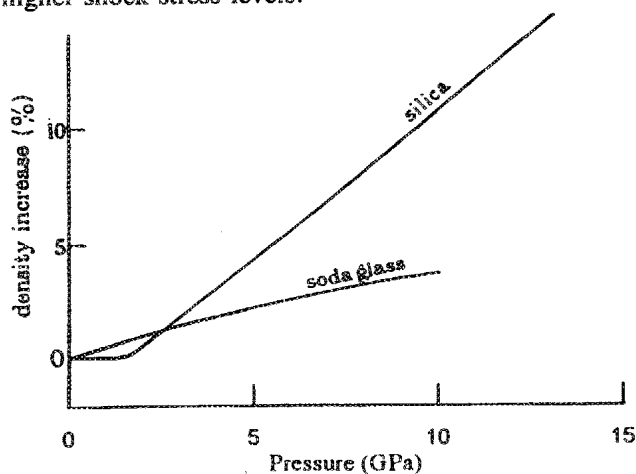


FIGURE 6. Graph showing the densification of soda glass and fused silica [22].

### 3.2. Elastic Shear and Dilatant Strain Energy Mechanism

Grady [18] proposed a mechanism to account for the observations on failure waves by assuming that an alternate pressure (mean stress) versus volume curve is initiated due to shear fracture induced dilatancy in the specimen which results in the failure wave formation, as shown schematically in Fig.5. He estimated the dilatant void volume,  $\Delta V_{di}$ , to accommodate the fracturing, relating the volumetric lattice strain  $\Delta V_{lat}/V$  due to a pressure change  $\Delta p$  through bulk modulus  $K$  as

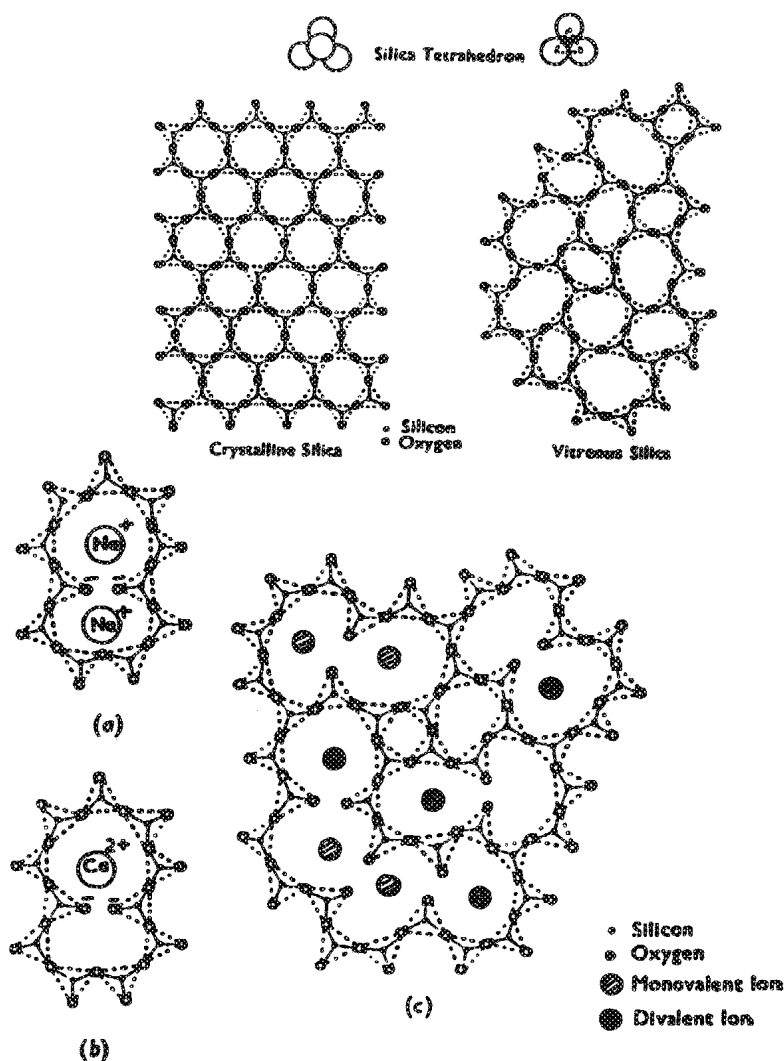


FIGURE 7. (above) Two-dimensional representation of the silica tetrahedron and of crystalline and vitreous silica. The silica tetrahedron is drawn to the scale of the ionic radii of the oxygen and silicon. In the right-hand tetrahedron the top oxygen has been removed to show the silicon atom. The lower diagrams are on the same scale but only the centers of the atoms are indicated for sake of clarity. Again the top oxygen atoms have been omitted. (below) Two-dimensional representation of a silicate glass (soda lime) containing modifying ions, illustrating the way in which (a) a monovalent oxide and (b) a divalent oxide goes into the silica network; (c) represents part of a network containing

several modifying ions.

$$\Delta p = -K(\Delta V_{lat}/V_{lat}).$$

Since the total volume strain,  $\Delta V$ , across the failure wave is zero,  $\Delta V_{dil}$  is given by

$$(\Delta V_{dil}/V) \approx \Delta p/K.$$

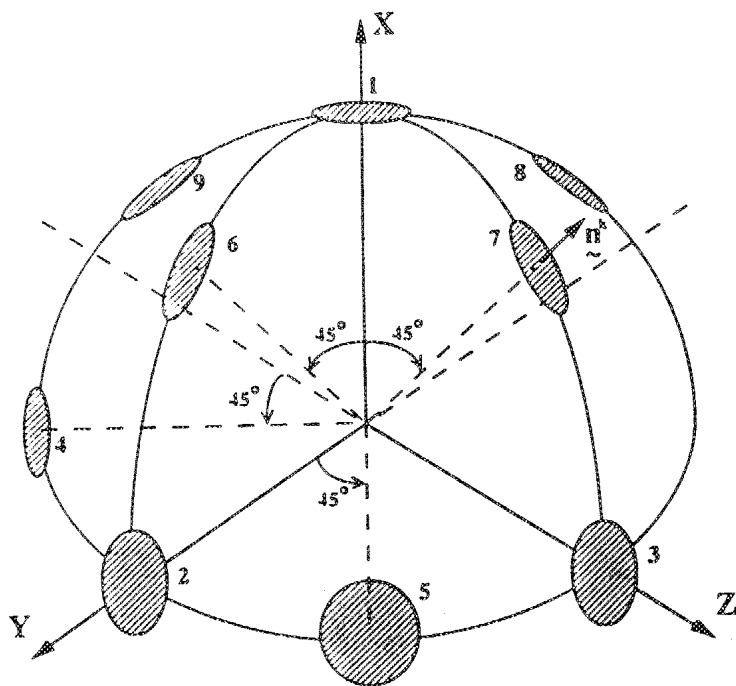


FIGURE 8. Configuration of the Multiple-plane Model [19].

Assuming further that  $\Delta\sigma_x = 0$  and that  $(\sigma_x = \sigma_y)$  behind the failure wave, then  $\Delta p \approx 4\tau/3$ , where  $\tau$  is the shear stress in the elastic state of the material in front of the failure wave. He calculated the value of  $\Delta V_{dil}$  to be about 4% for glass shocked to 5 GPa on Hugoniot, using nominal values of  $\tau = 1.7$  GPa and  $K = 56$  GPa. He concluded that the complete transfer of elastic shear strain energy to dilatant strain energy yields a comparable result.

The amount of dilation needed to explain the observed loss of shear and spall strengths due to failure waves is about 0.670 if the observed inhomogeneous deformation of silicate glasses is considered in conjunction

with microfracturing as shown in Appendix A. The analysis is carried out for two cases, one where glass loses its shear strength completely and the second when glass loses the shear strength partially. The flow stress of soda-lime glass at room temperature was estimated by Marsh from his indentation experiments to be in the range of 1.7 to 1.8 GPa [22,23]. These levels of average shear stress are generated when soda lime glass specimens are subjected to shock stress of 5 GPa, as shown in the calculations in Appendix A. The magnitude of shear stress is amplified at the microscopic defects and leads to the formation of nucleation sites for inelastic deformation. The inelastic deformation at these sites accompanied by stress relaxation will lead to pervasive shear failure of the material. The shear failure in glass specimens is likely to lead to a network of microcracks as a result of relaxation of internal shear stresses. Consequently the tensile and shear strength of the shocked glass specimen will be reduced. The expected lower flow stress at higher specimen temperature during the passage of the elastic shock will also favor local inelastic deformation significantly.

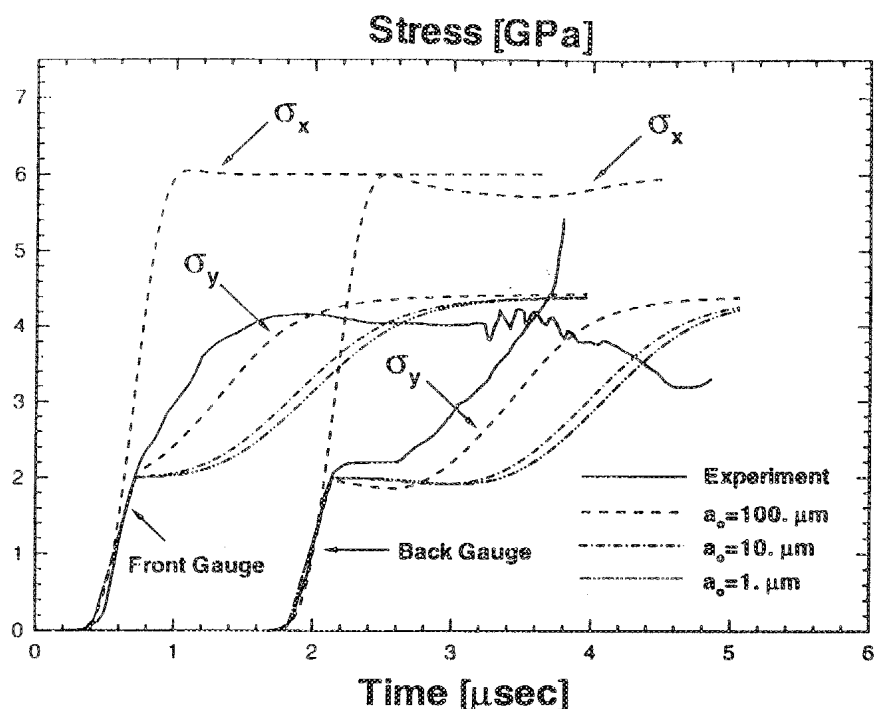


FIGURE 9. Transverse stress histories from experiment 7-1719. Comparison between experimental profiles and simulation with three different initial crack sizes. Lateral and axial stresses are plotted for the case  $a_0 = 100 \mu\text{m}$ .

### 3.3. Inhomogeneous Inelastic Behavior of Glass

Espinosa [19] and Espinosa et al. [20] proposed that the formation of the failure waves is mainly due to the unique inelastic behavior of silicate glasses. The mechanism involves the plastic flow behavior of glasses and, therefore, we first present a brief overview on this property of silicate glasses. Failure waves have been observed only in silicate glasses (soda lime, borosilicate, and aluminosilicate) of compositions containing silica network modifier ions such as  $B^+$ ,  $Na^+$ ,  $Ca^{++}$ , etc., and not in pure silica glass or fused quartz, the structure is likely to play a dominant role in the origin of the observed failure waves. The amount and type of network modifier in the silica structure in different glasses drastically affect their mechanical behaviors, especially the plastic flow and fracture characteristics. For example, Young's modulus of soda lime glass decreases with increasing strain ( $dE/d\epsilon < 0$ ) while that of fused silica increases with increasing strain ( $dE/d\epsilon > 0$ ) [24]. Secondly, fused silica undergoes mainly densification on compression, whereas silicate glasses show slight densification accompanied by considerable plastic deformation on compression. Marsh compared the densification data on soda glass [25] to those of fused silica [26] and found that under a confining quasi-hydrostatic pressure of 10 GPa fused silica densities by 12% and soda glass by 3.5% (Fig. 6) [23].

Marsh [22,23] in a comprehensive study of plastic flow and fracture in silicate glasses postulated that glass being random structurally, and hence, presumably a non-work-hardening solid, has no stabilizing mechanism at the yield point and so must fail catastrophically when the applied stress reaches the flow stress. Silicate glasses can be considered to consist of hard ordered regions about 2 nm in diameter separated by softer, disordered regions, and by analogy with grain boundary sliding, one may expect any flow to involve large and incompatible strain in the softer material. The flow would need to involve an area comparable to this substructure size to become meaningful, and this gives us a critical plastic zone size.

Ainsworth [27] interpreted the hard ordered and softer disordered regions in glass on the basis of the silica network "modifiers" such as soda ( $Na_2O$ ) and lime ( $CaO$ ) present in the basic silica structure, as shown in Fig. 7. With the addition of network modifiers the oxygen links at the silica tetrahedrons corners are broken. For a combined total of 33% soda and lime, the oxygen link at one corner of each silica tetrahedron is broken. For a further increase in the soda and lime concentration a second bridge of some of the tetrahedral is broken and with increasing "modifier" less and less tetrahedral are directly linked to other tetrahedral at three corners. The break in silica network form non-bridging oxygen ions which maintain relatively weaker bonds with  $Na^+$  and  $Ca^{++}$  ions compared to the stronger Si-O bond. These weaker bonds between  $Na^+$  and  $Ca^{++}$  ions with  $O^-$  ions form

the softer disordered regions and consequently lower the flow stress of soda lime glass compared to that of pure silica glass. Based on this argument Ainsworth suggested that the flow strength of soda lime and other similar glasses is directly related to the proportion of network modifiers in the silica structure.

Ernsberger [28] suggested the working hypothesis that plastic flow in glasses occurs by an inhomogeneous mechanism. Large shear displacements occur on certain planes, but only elastic strain occur between the planes. The favored planes on which shear displacements are presumably nucleated have some weak points in the network. These weak points are likely to lie in the softer regions formed at the bonds between the non-bridging  $O^-$  ions and the  $Na^+$  and  $Ca^{++}$  ions. Soda-lime glass contains  $Ca^{++}$  and  $Na^+$  ions, which provide ionically-bonded interfaces between the silica tetrahedral formed by covalent bonds between Si and O ions. The shear does not occur in the siloxane network itself because of the strong covalent bonds that make the silica tetrahedral. In other words, the siloxane network forms the relatively harder regions in glass according to the terminology of Ainsworth [27]. It undergoes only densification under compression as shown by Peter [29], since there is no evidence of plastic deformation. The shear deformation possibly leads to shear cracking around local weaker regions in glass that collapse. According to Ernsberger [28] the dimensions of the slip bands are large enough to rule out the role of cracks in the deformation.

According to Argon[30] the local shear strain in glasses require relative displacements between neighboring atoms. Since glassy materials are disordered on the atomic scale and contain a distribution of free volume, local shears do not effect the surroundings as strongly as in a perfect crystal and are in many instances locally accommodated without propagating out. This permits mechanically isolated large local shears in small individual elements of "loose" atomic packing. Thus, plastic deformation in glassy materials is still a non-local form of deformation in comparison with elastic deformation but can be far more local than the corresponding form in crystalline matter involving propagating dislocations.

Based on the above discussion on the shear behavior of silicate glasses Espinosa [19] and Espinosa et al. [7,20] proposed the following hypothesis to numerically simulate the failure wave. Penny-shaped defects are nucleated in the material due to inhomogeneous shear deformations produced in the shock compressed glass specimens. The failure wave is modeled as a propagating inelastic boundary. This is accomplished by nucleating penny-shaped defects, with initial size  $a_0$ , on elements located behind the failure front that initiates at the impact surface of the specimen and propagates into its interior. The evolution of these defects is modeled based on equations presented in the next section.

**3.3.1. Microcracking Multiple-Plane Model.** The inelastic response of glass is modeled through a microcracking multiple-plane model based on a dilute approximation (Taylor model). Our formulation overlaps some theories in which multiple-plane representations of inelasticity are derived, e.g., Seaman and Dein [31], Bazant and Gambarova [32], Ju and Lee [33]. In the quasi-static case, Ju and Lee [33] employed a self-consistent method together with analytical solution for weakly interacting cracks in order to derive inelastic compliance's. Unfortunately, the average methods used to compute effective moduli do not allow a straightforward extension into the dynamic problems.

The basic assumption in the microcracking multiple-plane model derived by Espinosa [34] is that microcracking and/or slip can occur on a discrete number of orientations as shown in Fig.8. Slip plane properties (friction, initial size, density, etc.) and their evolution are independently computed on each plane. The macroscopic response of the material is based on an additive decomposition of the strain tensor in an elastic part and an inelastic contribution arising from the presence of microcracks within the specimen. In contrast to scalar representations of damage, e.g., Rajendran [35], Espinosa's formulation is broad enough to allow the examination of *damage induced anisotropy* and damage localization in the interpretation of impact experiments.

For a representative volume  $V$  of an elastic solid containing penny-shaped microcracks with a density  $N^{(k)}$ , the average inelastic strains are given by

$$\epsilon_{ij}^c = \sum_{k=1}^9 N^{(k)} S^{(k)} \frac{1}{2} (\bar{b}_1^{(k)} n_j^{(k)} + n_1^{(k)} \bar{b}_j^{(k)}), \quad (1)$$

where the subindex  $k$  is used to label the orientations,  $S^{(k)}$  denotes the surface of a microcrack on orientation  $k$ ,  $n^{(k)}$  the corresponding unit normal, and  $(b)^{(k)}$  the average displacement jump vector across  $S^{(k)}$ .

If the resolved normal traction acting on the microcracking on orientation  $k$  is tensile, the average displacement jump vector resulting from an applied stress field  $\sigma$  is given by

$$\begin{aligned} \bar{b}_i^{(k)} &= \frac{1}{S^{(k)}} \int_{S^{(k)}} \bar{b}_i^{(k)} ds = \\ &= \frac{16(1-\nu^2)}{3E(2-\nu)} a^{(k)} (2\sigma_{ij} n_j^{(k)} - \nu \sigma_{ij} n_j^{(k)} n_1^{(k)} n_i^{(k)}) \end{aligned} \quad (2)$$

in which  $E$  and  $\nu$  are the Young's modulus and Poisson's ratio of the uncracked solid, and  $a^k$  is the radius of the penny-shaped microcracks on orientation  $k$ . By contrast, if the normal traction is compressive, the



microcracks are closed and the average displacement jump is given by

$$\bar{b}_i^{(k)} = \frac{32(1-\nu^2)}{3\pi E(2-\nu)} a^k \mathbf{f}_i^k \quad (3)$$

where  $\mathbf{f}^k$  is the effective shear traction vector on orientation  $k$  is given by

$$\mathbf{f}_i^k = (\tau^k + \mu\sigma_n^k)(\mathbf{n}_r)_i^k \quad (4)$$

in Eq.(4),  $\mu$  is the friction coefficient of the microcrack faces,  $\tau^k$  and  $\sigma_n^k$  are the resolved shear stress and the normal stress acting on microcracks with orientation  $k$ , respectively, and  $\mathbf{n}_r^k$  is the unit vector in the direction of the resolved shear traction. Embodied in Eq.(3) is the notion that  $\mathbf{f}^k$  provides effective driving force for the sliding of the microcracks.

In order to compute the inelastic strain tensor at all times, it becomes necessary to follow the evolution of the microcrack radius  $a^k$  in the selected orientations. Following Freund [36], an equation of evolution for  $a$  in the case of mixed mode loading can be derived, viz.,

$$\dot{a}^k = m^\pm c_R [1 - K_{IC}/K_{eff}^k]^{n^\pm} \geq 0, \quad (5)$$

in which  $n^\pm$  and  $m^\pm$  are phenomenological material constants which may have different values in tension and compression,  $c_R$  is the Rayleigh wave speed,  $K_{IC}$  is the material fracture toughness, and  $K_{eff}^k$  is an effective stress intensity factor. For mixed mode conditions,  $K_{eff}^k$  is derived by considering an average energy release rate associated with an increase in radius of the microcracks, namely,

$$G^k = \frac{1}{2\pi} \int_0^{2\pi} \frac{1-\nu^2}{E} [K_I^2 + K_{II}^2 + K_{III}^2 / (1-\nu)] d\theta \quad (6)$$

from which the following expression for  $K_{eff}^k$  obtained

$$K_{eff}^k = \sqrt{\frac{G^k}{1-\nu^2}} \quad (7)$$

The general structure of these constitutive equations corresponds to that of a solid with a damage-induced anisotropic stress-strain relation with elastic degradation. In particular, the effective behavior of the solid is predicted to be rate dependent due to crack kinetics effects. From a computational standpoint, this ensures numerical reliability and mesh independence (Needleman [37], Espinosa [38]). This is in contrast to quasi-static formulations of damage for which the governing equations become ill-posed in the

softening regime (Sandier and Wright [39]). If the material is subjected to a predominantly tensile stress state, microcracks along orientations perpendicular to the direction of maximum tensile stresses will grow according to Eq. (5). In this case, significant dilation is expected due to mode I crack opening. If a predominantly compressive state of stress with shear is imposed, then crack opening is inhibited but inelasticity is manifested by the growth of penny-shaped cracks in modes II and III (shear modes).

#### 4. MODEL SIMULATIONS AND COMPARISON

In this section we reproduce the numerical simulations performed by Espinosa et al. [20] using the model described above. Normal impact and pressure-shear impact are modeled to gain insight on the failure mechanisms in silicate glasses.

##### 4.1. Lateral Gauge Profile Simulations

The microcracking multiple-plane model discussed above has been utilized in the interpretation of the plate impact experiments conducted on glass specimens. A dynamic finite element analysis is performed to simulate the experiments reported in Espinosa et al. [20]. In all the calculations reported here, the failure wave phenomenon is modeled as a propagating damage boundary. This is accomplished by activating the microcracking model on elements located within a damage region defined by a failure front that initiates at the sample surfaces and propagates to its interior. The set of model parameters used in the calculations are  $N = 10^{11} \text{ m}^{-3}$  on all nine planes,  $K_{IC} = 0.5 \text{ MPa} \cdot \text{m}^{1/2}$ ,  $\mu = 0.15$ ,  $a_0 = 1 \text{ } \mu\text{m}$ ,  $n^+ = m^+ = 0.3$ , and  $n^- = m^- = 0.1$ . When the values of these parameters are changed, the corresponding plots indicate the variation with respect to these values. Other parameters like crack density are selected such that they are in agreement with the observations performed on recovered samples, see Espinosa et al. [20]. In fact, Espinosa et al. [20] reported an average fragment size  $d = 150 \text{ } \mu\text{m}$  which results in a crack density (assuming only three active orientations) of approximately  $1/(3d^3) = 0.99 \cdot 10^{11} \text{ m}^{-3}$  on each orientation. When such information is not experimentally available, the density is selected consistent with the impact surface roughness. For highly polished surfaces, a crack density of  $10^{11}$  is utilized, while for intentionally roughened surfaces (pressure-shear configuration),  $N = 10^{13}$  is used.

Numerical simulations of the lateral gauge configuration, experiment 7-1719 [20] are shown in Fig. 9. The measured transverse stresses, through lateral manganin gauges, are compared to the computed stresses for three different values of initial crack size. It can be observed that the stress increase resulting from crack growth, under fully compressive stresses,

exhibits different rates as a function of  $a_0$ . For  $a_0 = 1 \mu\text{m}$  the rate of lateral stress increase, at the location of the front gauge, is smaller than the one recorded experimentally. Furthermore, the lateral stress increase upon arrival of the failure wave, at the back gauge, presents a delay with respect to the experimental record. This delay is the result of crack kinetics effects rather than failure front speed. In all calculations the failure front is assumed to propagate at 2 km/s. When the initial crack size is increased to 100  $\mu\text{m}$  better agreement is obtained. These observations appear to indicate that the propagating failure front consists of the sweeping of propagating defects rather than the nucleation of new ones. In the present simulations,  $a_0$  is the initial crack size nucleated behind the failure front and should not be interpreted as an initial defect in the intact material. The numerically predicted axial stress,  $\sigma_x$ , is also plotted in Fig.9 for the case  $a_0 = 100 \mu\text{m}$ . A progressive reduction in axial stress is predicted.

#### 4.2. Normal Impact Spall Experiments Simulations

Normal impact experiments investigating the existence of failure waves have been reported by Raiser and Clifton [40]. In their experiments the interaction of an unloading wave, from the back surface of a target glass plate, with the advancing failure front was monitored by means of free surface interferometric measurements. Depending on the impactor thickness, spall planes in front and behind the failure front were produced. In Fig.10, the computed and experimentally recorded free surface velocities for the case in which tensile loading is produced in front of the failure wave are shown. A difference in the rising part of the free surface velocity results because glass densification is not incorporated in the present model. Such densification results in a nonlinear material behavior which is manifested by the attenuation of the wave front and the generation of a tail following stress release. Since our main interest is the identification of the failure wave mechanism, we will not account for glass densification in our modeling. From the computed velocities, it is clear that interaction of the unloading wave with the advancing failure front generates waves that result in a reacceleration of the target free surface. In the simulations, two different values of  $n^+$  (see Eq.(17) in [14]) have been used to assess the effect of crack growth rate in the free surface velocity. The smaller crack tip velocity (smaller  $n^+$ ) seems to provide the best fit of the experimental record. The rate of free surface velocity increase is well captured by this simulation. When a higher crack speed is used, the arrival of the second unloading wave, at approximately 1.3  $\mu\text{s}$ , does not become evident in the profile, and the overall reacceleration is excessive.

From these calculations, one can conclude that the free surface reacceleration is produced by crack growth behind the failure front when the

material is subjected to tensile dynamic loading. A relevant feature to note

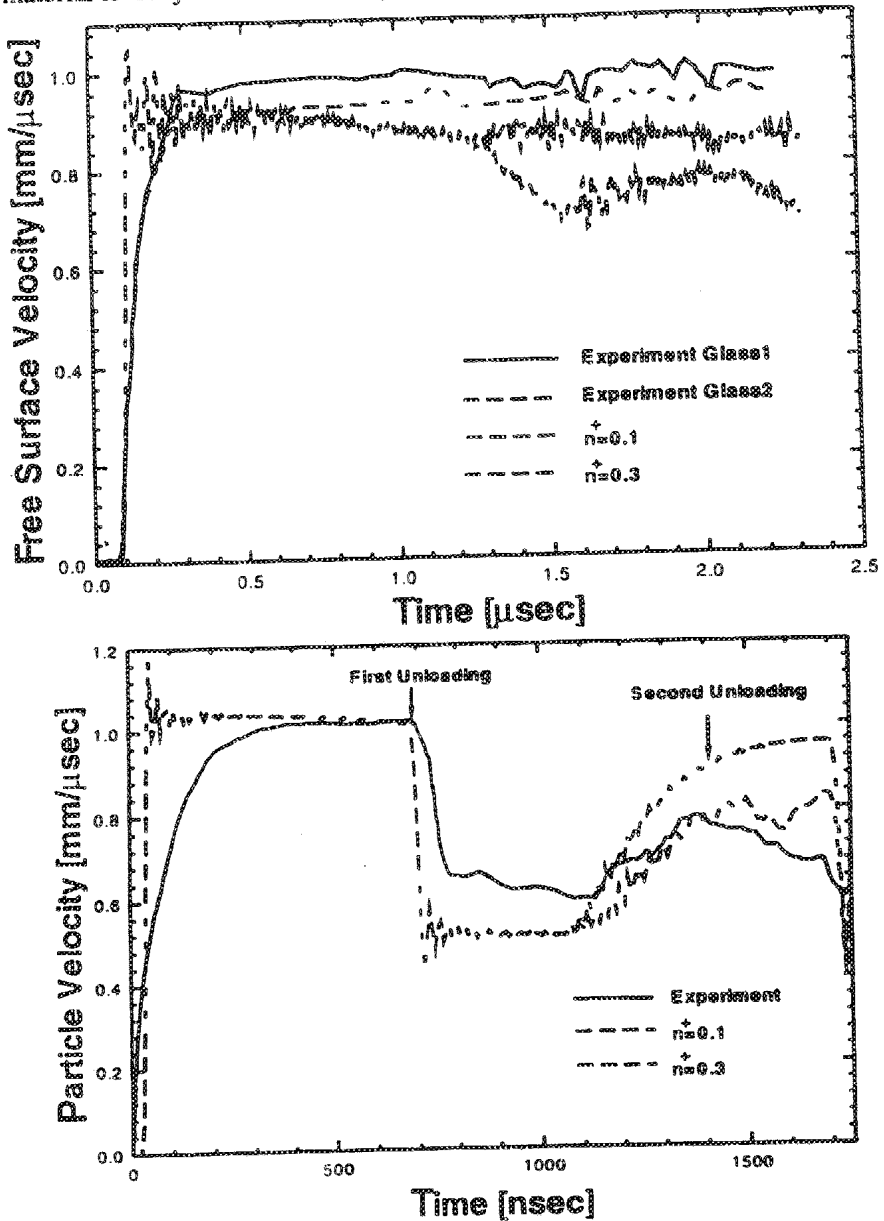


FIGURE 10. (above) Free surface particle velocity prediction for experiment GLASS2. The velocity history for experiment GLASS1 is also shown in the same figure [8]. An almost complete loss of spall strength is predicted at  $n^+ = 0.3$ . (below) Free surface particle velocity prediction for experiment 93-04 [40]. Increase in particle velocity after initial unloading is due to progressive

spallation of glass.

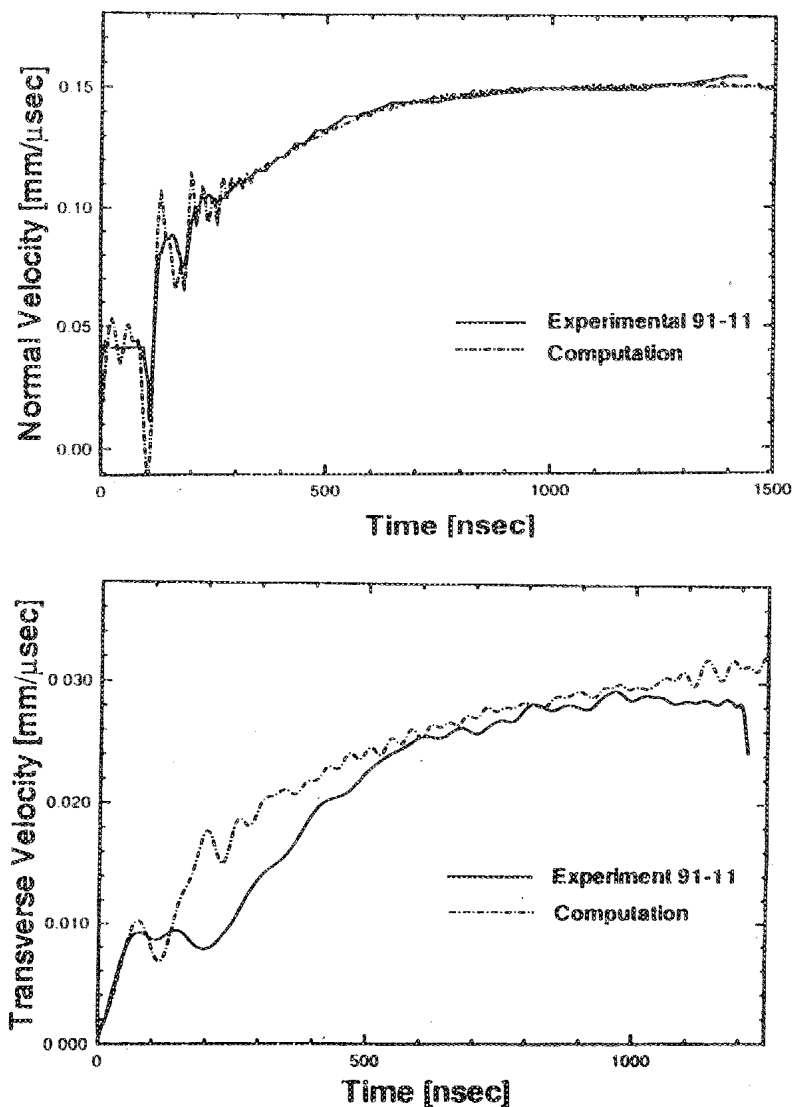


FIGURE 11. Comparison of numerical simulation and measured normal velocity (above) and transverse velocity (below) histories from high strain rate pressure-shear experiment 91-11 [20].

is that the increase in free surface particle velocity is progressive; i.e., the material behind the failure front has a reduced but finite spall strength. The case in which the two unloading waves, one from the target back surface and the other from the impactor back surface, meet behind the failure front

is also examined in Fig. 10. The experimental profiles show a fast increase in velocity followed by a plateau with a free surface velocity of 0.9 km/s. In the case of experiment GLASS2, a small reacceleration, at approximately 1.1 km/s, instead of a velocity reduction, is reported in [40]. This feature indicates that the material located at a distance from the failure front exhibits an almost complete loss in spall strength. In experiment GLASS 1, a small reduction in free surface velocity is observed at a time corresponding to the arrival of the unloading wave. When the computed velocity is compared to the experimental record, once again, there is an initial difference in particle velocity due to the fact that our model does not address glass densification. An almost complete lack of spall strength is predicted in our model when  $n^+ = 0.3$  is used in the equation for crack evolution. By contrast, when a smaller crack tip velocity is used in the simulations, the material behind the failure front presents a reduced but finite spall strength. It should be noted that the nonlinear behavior induced by glass densification will in general produce a pulse tail that could reduce the decrease in particle velocity observed in the case in which  $n^+ = 0.1$ . Hence, it appears that modeling of glass densification will provide a more accurate interpretation of these experimental records. Another feature revealed by the numerical simulations is a slow decay in free surface particle velocity after the initial rising part. This decay seems to be linked to the accumulation of inelasticity behind the failure front. Although this feature is not present in the experimental traces reported in Raiser and Clifton [40], recent experiments performed by Dandekar and Beaulieu [14] and Grady [15] appear to confirm our numerical prediction.

#### 4.3. Pressure-Shear Experiments

Direct experimental information concerning the shear resistance of Corning glass was obtained by means of pressure-shear high strain rate experiments [41]. The normal and transverse velocities recorded for Shot 91-11 are given in Fig. 11. The existence of a gap at the glass-flyer interface is evident from the partial unloading of the normal wave after 95 ns. Upon closure of the gap, the normal velocity monotonically increases up to the attainment of a state of homogeneous deformation. A maximum normal stress of 8 GPa is achieved well above the reported threshold stress for the formation of failure waves.

Hence, since the sample thickness is only 300  $\mu\text{m}$ , we expect the failure wave to propagate through the entire sample by the time the homogeneous deformation state develops. The shear wave profile shows an increase in stress to a level of about 200 MPa with a small stress reduction after 200 ns, resulting from the reduction in normal stress at the specimen-anvil interface. Subsequently, the shear stress rises to a plateau value of 880

MPa. This stress level is well below the stress level predicted by one dimensional elastic wave theory which clearly shows the achievement of a state of inelastic deformation in the glass specimen. An important implication of these measurements is the fact that the measured shear stress during the state of homogeneous deformation,  $\tau = 0.88$  GPa, is in close agreement with the shear stress behind the failure wave measured in normal impact experiments reported in [5,6, 10]. This feature implies that the shear stress interferometrically recorded in the pressure-shear experiments corresponds to the dynamic behavior of damaged glass. We examine this point by performing numerical simulations of this experiments with a microcracking multiple-plane model. The simulated normal and transverse velocities, as shown in Fig.11, show a good agreement with the measured velocities. Further numerical computations using the multiple-plane model will be performed on the pressure shear experiments on glass currently being pursued in our laboratories. Another feature revealed by the pressure-shear experiments, that the shear resistance of aluminosilicate glass increases from 700 MPa to 880 MPa when the pressure increases from 6 GPa - 9.6 GPa, will also be examined through numerical simulations.

## 5. CONCLUSIONS

Identification and modeling of failure waves in glass have been the objective of a number of recent investigations [1,17-20]. We have addressed the failure process by means of a microcracking model based on the observed plastic flow behavior of silicate glasses to obtain insight into the micromechanics of the failure event. Since under fully compressive stress states generated in plate impact experiments, differences between plastic flow in narrow bands and crack propagation under Modes II and III are more mathematical than physical, but the numerical simulations are consistent with both microcracking and shear-activated flow (inhomogeneous plastic flow) mechanisms. The main difference between these two hypotheses is that in the former cracks are generated at the start of the compressive pulse, while in the later cracks are formed at a later time at the intersection of flow surfaces. Physically, in the shear-induced flow mechanism the network of discontinuities behind the failure front exhibits tensile strength. The numerical simulations presented in the paper are consistent with previous experimental observations; although, a reduced but finite spall strength is predicted for small crack tip velocities even at locations well behind the failure front. The progressive spallation of glass at the failure front and its vicinity is accurately captured by the model. The available experimental data on failure waves in silicate glasses (Section 1) are analyzed in their totality, the shear-activated flow mechanism appears more likely than the microfracture mechanism. We have noted in the discus-

sion of lateral gauge experiments, that the failure wave seems to consist of the sweeping of propagating defects, presumably planar, rather than the nucleation and growth of new defects. Moreover, when the previously mentioned progressive spallation behind the failure front is taken into consideration, it appears reasonable to postulate the nucleation, at the intersection of flow planes, and subsequent growth of microcracks with accumulated inhomogeneous flow in the material. If the failure wave is interpreted as the propagation of a system of cracks from the impact surface to the interior of the specimen, an inconsistency with the observed progressive spallation immediately behind the failure front arises.

## APPENDIX A

Assume a shock stress ( $\sigma_1$ ) of 5 GPa is introduced in a glass target. Determine the strain ( $\epsilon_1^f$ ), transverse stress ( $\sigma_2^f$ ), maximum shear stress ( $\tau^f$ ), mean pressure  $P^f$ , in the glass target in front of the failure wave. For soda lime glass  $E = 71.3$  GPa,  $G = 29.3$  GPa, and Poisson's ratio ( $\nu$ );  $K = E/3(1-2\nu) = 42.4$  GPa. Compression  $\epsilon_1^f$  (in the elastic range for  $\sigma_1 = 5$  GPa)  $= 5/(42.4 + 4/3 * 29.3) = 0.061$ ; transverse stress  $\epsilon_2^f = (\sigma_1 * \nu)/(1-\nu) = 5*0.22/(1-0.22) = 1.4$  GPa; maximum shear stress  $\tau^f = 0.5(\sigma_1 - \sigma_2) = 0.5(5-1.4) = 1.8$  GPa; mean stress or  $P^f = (\sigma_1^f + \sigma_2^f)/3 = (5 + 2*1.4)/3 = 2.6$  GPa.

Behind the failure wave: According to Mallinder and Proctor (Physics and Chemistry of Glasses, Vol. 5, pp. 91-103 (1964) Young's modules  $E$  of soda lime glass decreases with the strain as  $E = 72.5(1 - 5.11\epsilon)$  GPa; for  $\epsilon = 0.06$ ,  $E^b = 72.5(1 - 5.11*0.06) = 50$  GPa; and for  $\epsilon = 0.05$ ,  $E^b = 72.5(1 - 5.11*0.05) = 54$  GPa.

Poisson's ratio  $\nu^b$  (of failed glass) behind the failure wave increases: Evidence (i) Mallinder and Proctor [24] find for fused silica by measuring  $E$  and  $G$  that  $\nu$  increases from 0.14 at zero strain to about 0.4 at a strain of 0.12. They modeled (phenomenological) this increase in terms of bending of rhombohedral links between Si and O ions; (ii) Our transverse gauge profiles in soda lime glass show an increase in  $\sigma_2$  on arrival of the failure wave. This increase in  $\sigma_2$ , in the elastic range of glass and without any change in  $\sigma_1$ , can only happen if the Poisson's ratio of the failed material (behind the failure wave) increases from 0.22 at zero strain to about 0.4 at  $\sigma_1 = 5$  GPa.

Determine  $K^b$  and  $G^b$  corresponding to  $\nu^b = 0.4$ :  $K^b = E^b/3(1 - \nu^b) = 50/3(1 - 2*0.4) = 84$  GPa and  $G^b = E^b/2(1 + \nu^b) = 50/2(1 + 0.4) = 18$  GPa.

Using the values of  $K^b$  and  $G^b$ , the strain,  $\epsilon^b$ , behind the failure wave is  $\epsilon^b = \sigma_1/(k^b + 4/3 G^b) = 5/(84 + 4/3*18) = 0.046$  [since  $\sigma_1$  is same in front of and behind the failure wave) and  $\sigma_2 = \nu^b * \sigma_1/(1 - \nu^b) = 5*0.4/(1 -$



0.4) = 3.33 GPa. Maximum shear stress  $\tau^b = 0.5(\sigma_1 - \sigma_2) = 0.5(5 - 3.33) = 0.84$  GPa. Note: This value of  $\tau^b$  agrees well with the measured value by us and Bourne et al. Mean stress  $P^b = (\sigma_1 + 2\sigma_2)/3 = (5 + 2 \cdot 3.33)/3 = 3.9$  GPa. There is an increase in the mean stress by 1.3 GPa.

The strain  $\epsilon^b$  in the glass behind the failure wave can be calculated by assuming: (i) glass has lost the shear strength completely and behaves like a fluid or (ii) it has reduced shear strength. Thus, according to the first assumption  $\epsilon^b = P^b/K^b = 3.9 \text{ GPa}/84 \text{ GPa} = 0.046$  and based on the second assumption  $\epsilon^b = \sigma_1/(K^b + 4/3 G^b) = 5/(84 + 4/3 \cdot 18) = 0.046$  same as in case (I). Based on the observations (VISAR and manganin gauge)  $\sigma_1$  does not change and therefore the total strain in front of  $\epsilon^b$  and behind  $\epsilon^b$  the failure wave should remain the same. In order for this to be true, the extra volume (the difference between the strains in front of and behind the failure wave) should be accommodated in some way. The most likely mechanism is that the difference ( $0.061 - 0.46 = 0.014$ ) is accommodated in allowing the failed glass to dilate.

## REFERENCES

1. G.I.Kanel, S.V.Rasorenov, and V.E.Fortov, *The Failure Waves and Spallations Homogeneous Brittle Materials, Shock Compression of Condensed Matter- 1991*, S.C.Schmidt et al., Eds. (Elsevier Science Publ., 1992), p.451.
2. S.V.Rasorenov, G.I.Kanel, V.E.Fortov, and M.M.Abasehov, *High Pressure Research* **6**, 225 (1991).
3. N.S.Brar, Z.Rosenberg, and S.J.Bless, *J. de Physique IV, Coll. C3, Suppl. au J. de Physique III* **1**, C3-639 (1991).
4. N.S.Brar, Z.Rosenberg, and S.J.Bless, *Appl. Phys. Lett.* **59**, 3396 (1991).
5. S.J.Bless, N.S.Brar, G.I.Kanel, and Z.Rosenberg, *J. Am. Ceramic Soc.* **75**, 1002 (1992).
6. N.S.Brar and S.J.Bless, *High Pressure Res.* **10**, 773 (1992).
7. H.D.Espinosa and N.S.Brar, *Micromechanical Study of Inelasticity in Brittle and Amorphous Materials, proposal submitted to the Army Research Office* (1992).
8. G.F.Raiser, J.L.Wise, R.J.Clifton, D.E.Grady, and D.E.Cox, *J. Appl. Phys.* **75**, 3862 (1994).
9. G.F.Raiser, *Dynamic Failure Resistance of Ceramics and Glasses, Ph.D. Thesis*, (Brown Univ., Providence, RI 1994).
10. N.K.Bourne and Z.Rosenberg, *The Dynamic Response of Soda Lime Glass, Presented at the 1995 APS Topical Conference on Shock Compression of Condensed Matter* (Seattle, WA, August 13-18, 1995).
11. N.K.Bourne, Z.Rosenberg, and J.C.F.Millet, *J. Appl. Phys.*, (1994).
12. N.K.Bourne and J.C.F.Millet, *J. Appl. Phys.* (1994).
13. N.K.Bourne, Z.Rosenberg, and J.E.Field, *J. Appl. Phys.* **78**, 3736 (1995).
14. D.P.Dandekar and P.A.Beaulieu, *Failure Wave under Shock Wave Compression in Soda Lime Glass, Metallurgical and Materials Applications of Shock-Wave*

- and *High-Strain-Rate Phenomena*, L.E.Murr et al, Eds. (Elsevier Publ. 1995), p.211.
15. D.E.Grady, *APS Topical Conference on Shock Compression of Condensed Matter* (Seattle WA, August 13-18,1995).
  16. D.E.Grady, *Personal Communication* (1996).
  17. R.J.Clifton, *Appl. Mech. Rev.* **46**, 540 (1993).
  18. D.E.Grady, *Dynamic Properties of Ceramic Materials*, Sandia National Laboratory Report, SAND94-3266 (February 1995).
  19. H.D.Espinosa, *Fourth International Conference on Structures Under Shock and Impact IV*, N.Janes et al. Eds. (Computational Mechanics Publications, South-Hampton, UK, 1996), p.449.
  20. H.D.Espinosa, Y.Xu, and N.S.Brar, *J. Am. Ceram. Soc.*, (August 1996).
  21. R.V.Gibbons and T.J.Ahrens, *J. Geophys. Res.* **78**, 5489 (1971).
  22. D.M.Marsh, *Proc. Roy. Soc.* **A282**, 33 (1964).
  23. D.M.Marsh, *Proc. Roy. Soc.* **A279**, 420 (1964).
  24. F.P.Mallinder and B.A.Proctor, *Phys. and Chem. of Glasses* **5**, 91 (1964).
  25. H.M.Cohen and R.Roy, *J. Am. Ceram. Soc.* **44**, 523 (1961).
  26. J.D.Mackinzie and R.P.LaForce, *Nature* **197**, 480 (1963).
  27. L.Ainsworth, *J. Soc. of Glass Tech.* **38**, 501T (1954).
  28. F.M.Ernsberger, *J. Non-Crystal. Solids* **25**, 295 (1977).
  29. K.W.Peter, *J. Non-Crystal. Solids* **5**, 103 (1970).
  30. A.Argon, *Glass: Science and Technology, Elasticity and Strength in Glasses*, D.R. Uhlmann and N.J.Kreidl, Eds. (Academic Press, New York 1984), Vol.5, p.79.
  31. L.Seaman and J.L.Dein, *Proceedings of the IUTAM Symposium on Nonlinear Deformation Waves*, Tallin, Estonia, (Springer-Verlag, Berlin, 1983).
  32. Z.P.Bazant and P.G.Gambarova, *J. Struct. Engng., ASCE*, **110**, 2015 (1984).
  33. J.W.Ju and X.Lee, *J. Engng. Mech. ASCE* **117**, 1495 (1991).
  34. H.D.Espinosa, *Int. J. Solids and Structures* **32**, 3105 (1995).
  35. A.M.Rajendran, *High Strain Rate Behavior of Metals, Ceramics, and Concrete*, Air Force Report WL-TR-92-4006 (Wright-Patterson Air Force Base, OH, 1992).
  36. L.B.Freund, *Dynamic Fracture Mechanics* (Cambridge Univ. Press, UK, 1990).
  37. A.Needleman, *Comput. Meth. Engng* **67**, 69 (1988).
  38. H.D.Espinosa, *Finite Element Analysis of Stress Induced Damage in Ceramics*, M.Sc. Thesis (Brown University, Providence, RI, 1989).
  39. I.S.Sandier and J.P.Wright, *Strain-Softening-Theoretical Foundations for Large Scale Computations of Nonlinear Materials Behavior*, S.Nemat-Nasser et al. Eds. (Martinus Nijhoff, 1984), p.285.
  40. G.Raiser and R.J.Clifton, *High Pressure Science and Technology, Joint AIRAPT-APS Conference*, S.C.Schmidt et al., Eds. (Colorado Springs, CO, 1994), p.1039.
  41. H.D.Espinosa, *Micromechanics of the Dynamic Response of Ceramics and Ceramic Composites*, Ph.D. Thesis (Brown University, Providence, RI, 1992).